On periodically driven quantum systems
Tarasinski, B.M.

Cover Page

Universiteit Leiden

The handle http://hdl.handle.net/1887/43150 holds various files of this Leiden University dissertation.

Author: Tarasinski, B.M.
Title: On periodically driven quantum systems
Issue Date: 2016-09-20

6 Spin-orbit interaction in InSb nanowires

6.1 Introduction

Hybrid semiconductor nanowire-superconductor devices are a promising platform for the study of topological superconductivity.[7] Such devices can host Majorana fermions,[120,135] bound states with non-Abelian exchange statistics. The realization of a stable topological state requires an energy gap that exceeds the temperature at which experiments are performed (~50 mK). The strength of the spin-orbit interaction (SOI) is the main parameter that determines the size of this topological gap[154] and thus the potential of these devices for the study of Majorana fermions. The identification of nanowire devices with a strong SOI is therefore essential. This entails both performing measurements on a suitable material and device geometry as well as establishing theory to extract the SOI strength.

InSb nanowires are a natural candidate to create devices with a strong SOI, since bulk InSb has a strong SOI.[58,179] Nanowires have been used in several experiments that showed the first signatures of Majorana fermions.[40,44,46,128] Nanowires are either fabricated by etching out wires in planar heterostructures or grown bottom-up. The strong confinement in the growth direction makes etched wires two-dimensional (2D) even at high density. SOI has been studied in 2D InSb wires[86] and in planar InSb heterostructures,[87] from which a SOI due to structural inversion asymmetry,[144] a Rashba SOI α_R, of $0.03\,\mathrm{eV\mathring{A}}$ has been obtained.[87] Bottom-up grown nanowires are three-dimensional (3D) when the Fermi wavelength is smaller than the wire diameter. In InSb wires of this type SOI has been studied by performing spectroscopy on quantum dots,[129,132] giving $\alpha_R = 0.16 - 0.22\,\mathrm{eV\mathring{A}}$.[129] However, many (proposed) topological nanowires devices[79,80,178] contain extended conducting regions, i.e. conductive regions along the nanowire much longer than the
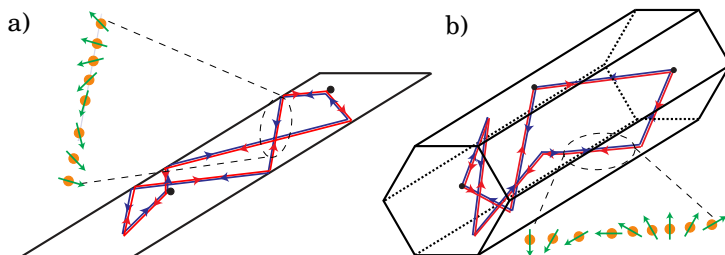
Figure 6.1: Quantum interference along time-reversed paths in 2D (a) and 3D (b) nanowires. In both cases an inversion symmetry induces spin precession in between (boundary) scattering events.

nanowire diameter. The SOI strength in these extended regions has not yet been determined. It is likely different from that in quantum dots, as the difference in confinement between both geometries results in a different effective electric field and thus different Rashba SOI. Measurements of SOI strength in extended InSb nanowire regions are therefore needed to evaluate their potential for topological devices. Having chosen a nanowire material, further enhancement of Rashba SOI strength can be realized by choosing a device geometry that enhances the structural inversion asymmetry.[56,133] Our approach is to use a high-k dielectric in combination with a top gate that covers the InSb nanowire.

6.2 Magnetoconductance measurements in 3D nanowires

The standard method to extract SOI strength in extended regions is through low-field magnetoconductance (MC) measurements.[78,81] Quantum interference (see Fig. 6.1) in the presence of a strong SOI results in an increased conductance, called weak anti-localization (WAL),[27] that reduces to its classical value when a magnetic field is applied.[10] From fits of MC data to theory a spin relaxation length is extracted. If spin relaxation results from inversion asymmetry a spin precession length and SOI strength can be defined. To extract SOI strength in nanowires the theory should contain (1) the length over which the electron dephases in the presence of a magnetic field, the magnetic dephasing length,[25] and (2) the relation between spin relaxation and spin precession length.[93] The magnetic dephasing and spin relaxation length depend, besides

magnetic field and SOI strength respectively, on dimensionality and confinement. For instance, in nanowires, the spin relaxation length increases when the wire diameter is smaller than the spin precession length [93,94,155]. Therefore the spin relaxation length extracted from WAL is not a direct measure of SOI strength. These effects have been studied in 2D wires, [25,93] but results for 3D wires are lacking. As geometry and dimensionality are different (see Fig. 6.1), using 2D results for 3D wires is unreliable. Thus, theory for 3D wires has to be developed.

In this chapter, we first theoretically study both magnetic dephasing and spin relaxation due to Rashba SOI in 3D hexagonal nanowires. We then use this theory to determine the spin-orbit strength from our measurements of WAL in dual-gate InSb nanowire devices, finding a strong Rashba SOI $\alpha_R = 0.5 - 1\,\mathrm{eV\,\mathring{A}}$.

The WAL correction to the classical conductivity can be computed in the quasiclassical theory as [25,37,106]

$$\Delta G = -\frac{e^2}{h}\frac{1}{L}\Big[3\Big(\frac{1}{l_\varphi^2} + \frac{4}{3l_{\mathrm{so}}^2} + \frac{1}{l_B^2}\Big)^{-\frac{1}{2}} - \Big(\frac{1}{l_\varphi^2} + \frac{1}{l_B^2}\Big)^{-\frac{1}{2}}$$

$$-3\Big(\frac{1}{l_\varphi^2} + \frac{4}{3l_{\mathrm{so}}^2} + \frac{d}{l_e^2} + \frac{1}{l_B^2}\Big)^{-\frac{1}{2}} + \Big(\frac{1}{l_\varphi^2} + \frac{d}{l_e^2} + \frac{1}{l_B^2}\Big)^{-\frac{1}{2}}\Big]. \qquad (6.1)$$

The length scales in this expression are the nanowire length L, the mean free path l_e, the phase coherence length l_φ, the magnetic dephasing length l_B, and the spin relaxation length l_{so}. The mean free path $l_e = v_{\mathrm{F}}\tau_e$ where τ_e is the mean time between scattering events and v_{F} the Fermi velocity. In addition, the remaining length scales are also related to corresponding time scales as

$$l_{B,\varphi,\mathrm{so}} = \sqrt{D\tau_{B,\varphi,\mathrm{so}}}. \qquad (6.2)$$

where $D = \frac{1}{d}v_{\mathrm{F}}l_e$ the diffusion constant in d dimensions ($d = 3$ for bottom-up grown nanowires).

In the quasiclassical theory, τ_φ (and hence l_φ) is a phenomenological parameter. In contrast, τ_B and τ_{so} are computed from a microscopic Hamiltonian, by averaging the quantum mechanical propagator over classical trajectories (the details of the theory are outlined in Sec. 6.3 below). τ_B and τ_{so} thus depend not only on microscopic parameters (magnetic field B and SOI strength, respectively), but through the average over trajectories also on dimensionality, confinement, and l_e. We
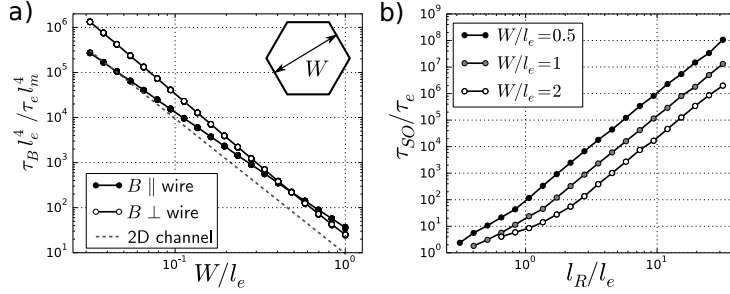
a)

b)

Figure 6.2: (a) Normalized dephasing time $\tau_B l_e^4/\tau_e l_m^4$ as a function of W/l_e for a hexagonal nanowire (see inset) for field parallel (black) and perpendicular (red) to the nanowire. Dots are numerical data for different l_m in the range $1 - 10^{2.5}$ ($10 - 20$ points per W), solid lines a fit to Eq. (6.3). Dashed line is the 2D wire result of Ref. 25. (b) τ_{so}/τ_e as a function of spin-orbit strength l_R/l_e and different wire diameters in a 3D hexagonal nanowire.

focus on the case where Rashba SOI due to an effective electric field in the z-direction, perpendicular to wire and substrate, dominates. Then the microscopic SOI Hamiltonian is $\frac{\alpha_R}{\hbar}(p_x\sigma_y - p_y\sigma_x)$, where $\sigma_{x,y}$ are Pauli matrices and $p_{x,y}$ the momentum operators. The corresponding spin-orbit precession length, l_R, equals $\hbar^2/m^*\alpha_R$. In our treatment we neglect the Zeeman splitting, E_Z since we concentrate on the regime of large Fermi wave vector, k_F, such that $\alpha_R k_F \gg E_Z$.

The quasiclassical description is valid if the Fermi wave length $\lambda_F \ll l_e, l_R$, and much smaller than the transverse extent W of the nanowire, i.e. for many occupied subbands. In particular, the quasiclassical method remains valid even if $l_R < l_e, W$.[185]

We evaluate τ_B and τ_{so} numerically by averaging over random classical paths for a given nanowire geometry. The paths consist of piece-wise linear segments of freely moving electrons with constant speed,[26,37] only scattered randomly from impurities and specularly at the boundary. These assumptions imply a uniform electron density in the nanowire. Specular boundary reflection is expected as our wires have no surface roughness.[181] (We extrapolate the results on InAsSb wires to InSb since the flatness of the facets results from the introduction of Sb.)

We apply our theory to nanowires with a hexagonal cross-section and diameter W (see inset in Fig. 6.2a) in the quasi-ballistic regime, $l_e \gtrsim W$. Fig. 6.2(a) shows the magnetic dephasing time τ_B (normalized by $\tau_e l_m^4/l_e^4$ with $l_m = \sqrt{\hbar/eB}$) as a function of wire diameter. Both parallel and perpendicular field give rise to magnetic dephasing due

to the three-dimensionality of the electron paths, in contrast to two-dimensional systems where only a perpendicular field is relevant (see Fig. 6.1). The different field directions show a different dependence on W, with, remarkably, τ_B (and thus l_B) independent of field-orientation for $W/l_e = 0.5$. Our results for τ_{so} as a function of l_R are shown in Fig. 6.2b. We find an increase of τ_{so} as the wire diameter W is decreased, indicating that confinement leads to increased spin relaxation times.

For $l_{m,R}, l_e \gtrsim W$ we can fit our results reliably as

$$\tau_{B,so} = C \frac{l_{m,R}^4}{W^\gamma l_e^{(4-\gamma)}} \,. \tag{6.3}$$

This is shown for τ_B in Fig. 6.2a where data for different l_m and W collapse to one line. In particular for τ_B, we find $C = 34.1 \pm 0.1$ and $\gamma = 2.590 \pm 0.002$ for parallel field, $C = 22.3 \pm 0.3$ and $\gamma = 3.174 \pm 0.003$ for perpendicular field. For τ_{so} $C = 8.7 \pm 0.5$ and $\gamma = 3.2 \pm 0.1$. Note that our numerics is valid beyond the range where the fit (6.3) is applicable. For example, for $l_R \lesssim W$ the numerical result deviates from the power-law of (6.3) as seen in Fig. 6.2b; in this regime only the numerical result can be used.

The fit (6.3) allows for a quantitative comparison of our 3D wire results to 2D wires: Both are similar in that there is flux cancellation $(\gamma > 2)$[25] and suppressed spin relaxation due to confinement. However, they exhibit a significantly different power-law. As an example, in Fig. 6.2a we compare to the 2D wire result for weak fields from Ref. 25 $(C = 10.8, \gamma = 3)$ that can differ by an order of magnitude from our results. This emphasizes the need for an accurate description of geometry for a quantitative analysis of WAL.

6.3 Evaluation of weak (anti-)localization in the quasiclassical theory

6.3.1 The quasiclassical theory

Within the quasiclassical formalism, the weak (anti-)localization correction ΔG is given as[26,37,106]

$$\Delta G = -\frac{2e^2}{\pi\hbar} \frac{D}{L} \int_0^\infty dt\, C(t)(1 - e^{-t/\tau_e}) e^{-t/\tau_\varphi} \langle \mathcal{M}_B(t) \rangle \langle \mathcal{M}_{so}(t) \rangle \tag{6.4}$$

In this expression, L is the length of the nanowire, $C(t) = (4\pi D t)^{-1/2}$ is the 1D return probability, $D = \frac{1}{d} v_F l_e$ the diffusion coefficient ($d = 3$ for the nanowires). $\langle \ldots \rangle$ denotes an average over all classical paths that close after time t. $\mathscr{M}_B$ is due to the orbital effect of the magnetic field and reads[37]

$$\mathscr{M}_B(t) = e^{i\phi(t)}, \text{ with } \phi(t) = \frac{2e}{\hbar} \int_{\boldsymbol{x}(0)}^{\boldsymbol{x}(t)} \boldsymbol{A} \cdot d\boldsymbol{l} . \qquad (6.5)$$

The Hamiltonian of spin-orbit interaction (SOI) can in general be written as

$$H_{\mathrm{SOI}} = \boldsymbol{\sigma} \cdot \boldsymbol{B}_{\mathrm{so}}(\boldsymbol{p}) \qquad (6.6)$$

where $\boldsymbol{\sigma}$ is a vector of Pauli matrices and $\boldsymbol{B}_{\mathrm{so}}$ a momentum-dependent effective magnetic field due to the SOI. In the case of Rashba SOI as considered here we have $\boldsymbol{B}_{\mathrm{so}}(\boldsymbol{p}) = \frac{\alpha_R}{\hbar}(-p_y, p_x, 0)$. The SOI of Eq. (6.6) then gives rise to the modulation factor[37,185]

$$\mathscr{M}_{\mathrm{so}}(t) = \frac{1}{2} \mathrm{Tr}\left(W(t)^2\right)$$

$$W(t) = \mathscr{T} \exp\left[\frac{i}{\hbar} \int_0^t dt' \boldsymbol{\sigma} \cdot \boldsymbol{B}_{\mathrm{so}}(\boldsymbol{p}(t))\right] \qquad (6.7)$$

where $\mathscr{T}$ is the time-order operator.

When the motion along the longitudinal direction of wire is diffusive, the modulation factors generally decay exponentially with time,[37]

$$\langle \mathscr{M}_B(t) \rangle = e^{-t/\tau_B}, \text{ and } \langle \mathscr{M}_{\mathrm{so}}(t) \rangle = \tfrac{3}{2} e^{-4t/3\tau_{\mathrm{so}}} - \tfrac{1}{2} . \qquad (6.8)$$

Note that τ_B and τ_{so} depend explicitly on the magnetic field B and the SOI strength through equations (6.5) and (6.7), respectively. However, through the average over classical paths, $\langle \ldots \rangle$ they also depend on the geometry of the nanowire and the mean free path l_e.

With the exponential form of the modulation factors in Eq. (6.8) the integral in Eq. (6.4) can be performed to give Eq. (6.1)

Requirements of the quasi-classical theory The quasiclassical description is valid if the Fermi wave length λ_F is much smaller than the typical transverse extent of the nanowire W, i.e. for many occupied subbands. It also requires that the classical paths are neither affected by magnetic field nor SOI: The former requires that the cyclotron

radius $\lambda_{\text{cyc}} \gg W, l_e$,[26,37] the latter that the kinetic energy dominates over the spin-orbit energy so that $l_R \gg \lambda_F$.[185] In particular, the quasi-classical method is valid also for $l_R < l_e, W$. Additional requirements are $\tau_B, \tau_{\text{so}} \gg \tau_e$, for the exponential decay of magnetic dephasing time (length) and spin relaxation time to be valid.[26,185] In addition we must have $l_\varphi \gg W$ to be in the quasi-one-dimensional limit, where the return probability $C(t)$ in Eq. (6.4) is given by the 1D return probability.

These are the fundamental requirements for the quasiclassical theory to hold. They should not confused with the stronger requirements $l_{m,R,e} \gtrsim W$ needed for the validity of the fit of Eq. (6.3)

Experimental fulfillment of quasi-classical requirements   The experimental details validating the applicability of the quasiclassical technique follow later in this chapter. The number of occupied subbands is discussed in Sec. 6.4.4. As shown in Fig. 6.5c below, l_φ largely exceeds the wire diameter for a large range of conductance, thereby obeying the requirement for a one-dimensional quantum interference model. The range of B (up to 200 mT) in the fits in Figs. 6.5 and 6.6 in general obey $\tau_B \gtrsim \tau_e$. Alternatively, fitting over a smaller B-range (up to $75 - 100$ mT, fulfilling $l_m \gtrsim W$, τ_e and $\lambda_{\text{cyc}} \gg W, l_e$ to a larger extent) can be performed on MC traces showing WAL without WL at larger B (observed when $G \geq 2e^2/h$) with fixed $\Delta G(B \to \infty)$, yielding the same results within $\sim 20\%$.

6.3.2 Monte Carlo evaluation

In order to obtain the decay times in Eq. (6.8) as a function of mean free path l_e, wire diameter W, and magnetic field B or Rashba spin-orbit strength α_R, we performed Monte-Carlo simulations of quasiclassical paths in a hexagonal nanowire, as has been described before in Refs. 26, 37 and 185.

Model and Boltzmannian ensemble   We model the nanowire as a three-dimensional prism of infinite length, with a regular hexagon as cross-section.

A Boltzmannian ensemble of quasiclassical paths is created, with each path consisting of propagation along a sequence of straight line segments with constant velocity. For each path, after certain intervals, the direction of the particles velocity is changed at random, with

isotropic distribution, corresponding to collision of randomly distributed pointlike impurities. The distance of free propagation between collision is determined at random, Poisson-distributed $P(l) \propto e^{-l/l_e}$, so that the mean-free path is l_e. On impact with one of the nanowires walls, reflection occurs in a specular fashion, by reversing the velocity component perpendicular to the wall. The resulting ensemble will consist of paths which are open (start and end point do not coincide).

Evaluation of $\mathcal{M}_B$, $\mathcal{M}_{so}$ After obtaining an ensemble of Boltzmannian paths, for each path the integrals Eq. (6.5) or Eq. (6.7) are evaluated. Because the paths consist of straight line segments, the evaluation is elementary for each segment, and the integrals $\mathcal{M}_B$, $\mathcal{M}_{so}$ are the products of these segments. For $\mathcal{M}_B$, these are the phase factors $e^{i\phi_n}$ accumulated along each segment, while for $\mathcal{M}_{so}$ we must multiply unitary two-by-two matrices which describe the spin dynamics along each segment. When calculating $\mathcal{M}$ at the same time as generating the path, only the last position, velocity and accumulated product of $\mathcal{M}_{B,so}(t)$ need to be kept in memory.

Magnetic field   To be more specific, for magnetic fields we choose the field to point along the y direction, and the nanowire to lie along either the x or y direction, so that the magnetic field is either perpendicular or parallel to the nanowires axis. In the perpendicular case, the orientation of the nanowire was either such that the magnetic field penetrated one of the faces perpendicularly, or such that it was parallel to one of the faces (the difference being a rotation by 30 degrees). It was established that for the resulting τ_B there is no significant difference between these two orientations in the relevant regime.

When choosing the gauge,

$$A(\boldsymbol{r}) = (Bz, 0, 0) \tag{6.9}$$

the generation of open paths is sufficient for the evaluation of $\mathcal{M}_B(t)$ according to Eq. (6.5), because the average $\langle \mathcal{M}_B(t) \rangle$ over open and closed paths is then identical.[25] Since open and closed paths are equivalent in this situation, we use open paths that are easier to generate numerically than closed paths. In our simulations, we chose an ensemble size of 2^{14} open paths to for averaging.

Spin-orbit   For $\langle \mathcal{M}_{so} \rangle$ an evaluation with open paths is not possible, and we have to average over an ensemble of closed paths, which is created as described in the following. By creating a number N of open paths of length $L/2$, we can create a set of $N(N-1)/2$ statistically independent open paths of length L, by pairwise concatenation of two different paths. We restrict this much larger set of paths to those which are almost closed (with start and end point separated not further than l_e), and then insert an additional line segment that closes these paths. If the concatenated paths are of sufficient length, we assume that the insertion of this additional line segment with a slightly different length distribution than the other line segments does not change the ensemble properties appreciably. Because we thus could only use a subset of the generated paths, we chose an ensemble size of 2^{16} open paths in this case. (The size of the ensemble of closed paths decreases with increasing L).

Fitting decay times   Finally, after having created ensembles of open or closed paths as described above for a set of different path lengths, which we chose to be logarithmically spaced, $t_n = (1.1)^n \tau_e$ with n integer and $1 \le t_n/\tau_e \le 10^6$, we determined the averages $\langle \mathcal{M}_{B,so}(t) \rangle$ and numerically fitted the exponential decays according to Eqs. (6.8), resulting in estimates for the decay times τ_B and τ_{so}.

Validating against known results: Square nanowire   To validate the results of our simulations for $\mathcal{M}_B$, we also simulate other geometries, in which results have been found previously, numerically or analytically. First, instead of considering hexagonal nanowires, we change the shape of the nanowire to be square. If a square nanowire is placed in a perpendicular magnetic field and has specularly reflecting walls, we expect the result to be the same as for a 2D layer, as treated in Ref. 25. This is because reflections on the walls perpendicular to B do not change the projection of the path along the direction of B, and thus are ineffective.

   We should thus reproduce the result of Ref. 25, which in the "clean, weak field" limit reads

$$\frac{\tau_B}{\tau_e} = 12.1 \frac{l_m^4}{W^3 l_e} \tag{6.10}$$

and should hold for $W \ll l_e$ and $l_m \gg \sqrt{W l_e}$. In the left frame of Fig. 6.3 we show simulation results for both perpendicular and parallel field
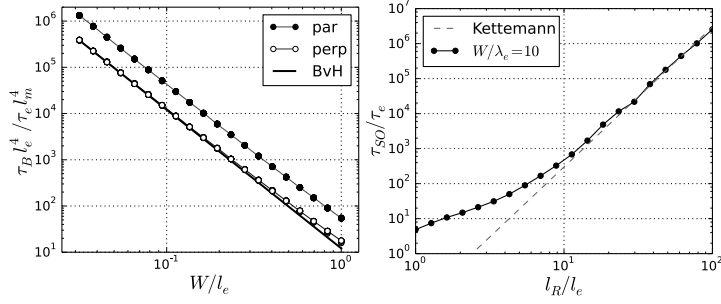
Figure 6.3: *Left:* Comparison to the analytical expression by Beenakker and van Houten.[25] Numerically obtained data points are shown for different magnetic field $l_e < l_m < 10^{1.5} l_e$, parallel ("par") and perpendicular ("perp") to the nanowire. The fact that points for different l_m collapse shows the expected l_m^4 behavior. The black line "BvH" is the asymptotic expression Eq. (6.10) for $W \ll l_e$. For $W \simeq l_e$, a cross-over to the diffusive regime can be observed. *Right:* Comparison of the numerical evaluation of $\langle \mathcal{M}_{so} \rangle$ in a 2D strip (blue dots and line) and the diffusive result of Ref. 93 (dashed line). In the numerics, the width of the strip is $W = 10\ell_e$, so that motion is diffusive. The Cooperon-based treatment in Ref. 93 applies for $l_R > W$.

for a square nanowire. In perpendicular field, the data agrees to the analytical results in the regime of its validity (the onset of cross-over to the diffusive case can be seen). Remarkably, in parallel field, we also observe a W^{-3} dependence, while for hexagonal geometry, the dependence on W^γ has two different γ for the two orientations.

Validating against known results: Spin-orbit coupling in 2D strip   To check the calculations of $\mathcal{M}_{so}$, we compare our simulations to the expression for τ_{so} for two-dimensional diffusive wires ($l_e \ll W$) with Rashba spin-orbit interaction from Kettemann.[93]

When comparing τ_{so} between different sources it is important to note that different conventions for τ_{so} exist (such as choosing a factor 4/3 in Eq. (6.8)). For consistency it is thus important to compare physical observables. For weak antilocalization this is the conductance correction. In order to describe the case of diffusive wires ($l_e \ll W$) we need to take the limit $l_e \to 0$ in Eq. (6.1):

$$\Delta G = -\frac{e^2}{h} \frac{\sqrt{D}}{L} \Big[3 \Big(\frac{1}{\tau_\varphi} + \frac{4}{3\tau_{so}} + \frac{1}{\tau_B} \Big)^{-\frac{1}{2}} - \Big(\frac{1}{\tau_\varphi} + \frac{1}{\tau_B} \Big)^{-\frac{1}{2}} \Big]. \qquad (6.11)$$

Kettemann uses a Green's function based approach and arrives at:[93]

$$\Delta G = -\frac{e^2}{h}\frac{\sqrt{D}}{L}\left[2\left(\frac{1}{\tau_\varphi}+\frac{1}{2\tau_{\mathrm{so}}^*}+\frac{1}{\tau_B}\right)^{-\frac{1}{2}}+\left(\frac{1}{\tau_\varphi}+\frac{1}{\tau_{\mathrm{so}}^*}+\frac{1}{\tau_B}\right)^{-\frac{1}{2}}-\left(\frac{1}{\tau_\varphi}+\frac{1}{\tau_B}\right)^{-\frac{1}{2}}\right],$$

(6.12)

where τ_{so}^* refers to the "τ_{so}" used in Ref. 93. In the limit of small spin-orbit splitting, $1/\tau_{\mathrm{so}} \to 0$, both expressions become equal if we identify

$$\tau_{\mathrm{so}} = 2\tau_{\mathrm{so}}^*.$$

(6.13)

Hence we need to take this factor of 2 into account when comparing our results to Kettemann's. Taking this factor into account, the expressions (6.11) and (6.12) not only agree for weak spin-orbit, but also never differ by more than 5% for all τ_{so}.

The right frame in Fig. 6.3 shows the comparison between the expression given in Ref. 93, which after conversion to the quantities used in this chapter is

$$\tau_{so}/\tau_e = 3l_R^4/W^2,$$

(6.14)

and numerical results we obtained for a diffusive 2D strip for different spin-orbit strengths.

6.4 Experiments

The experiments described below were performed in the QuTech lab and the Kavli Institute for Nanoscience in Delft, without direct involvement of the author of this thesis.

InSb nanowires[139] with diameter $W \approx 100\,\mathrm{nm}$ are deposited onto a substrate with a global back gate. A large ($\geq 2\,\mu\mathrm{m}$) contact separation ensures sufficient scattering between source and drain. After contact deposition a HfO_2 dielectric layer is deposited and the device is then covered by metal, creating an Ω-shaped top gate (Fig. 6.4a and insets of Fig. 6.4c-d). Nanowire conductance is controlled with top and back gate voltage, reaching a conductance up to $\sim 5e^2/h$ (Fig. 6.4b). The device design leads to a strong top gate coupling (Fig. 6.4c), while back gate coupling is weaker (Fig. 6.4d). From a field-effect mobility of $\sim$ 11,000 cm^2/Vs a ratio of mean free path to wire diameter $l_e/W = 1-2$ is estimated[140], see Sec. 6.4.2.
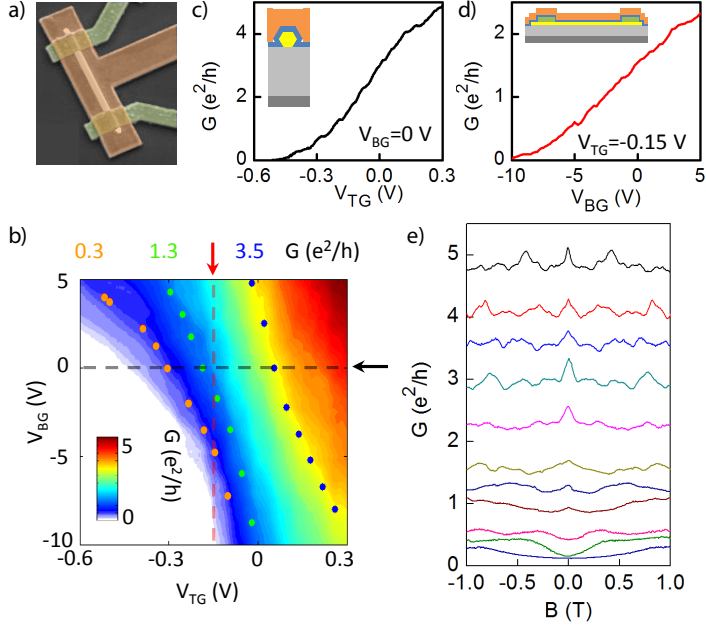
Figure 6.4: (a) False color scanning electron microscopy image of device I. Contact spacing is $2\,\mu m$. Device fabrication is described in Sec. 6.4.1 (b) Conductance G, as a function of top gate voltage, V_{TG}, and back gate voltage, V_{BG}. Arrows and dashed lines indicate cross sections shown in panels (c) and (d). Dots indicate voltages (V_{BG}, V_{TG}) at which traces in Fig. 6.5a were taken (same dot color corresponds to same G). Data taken with 10 mV voltage bias at a temperature of 4.2 K. (c) G as a function of V_{TG} at $V_{BG} = 0$ V. Inset: radial cross section of the device. The blue layer is HfO_2. (d) G as a function of V_{BG} at $V_{TG} = -0.15$ V. Inset: axial cross section of the device. (e) Conductance, as a function of magnetic field at several values of device conductance controlled by V_{TG}, $V_{BG} = 0$ V. Data taken with AC excitation $V_{AC} = 100\,\mu V_{RMS}$.
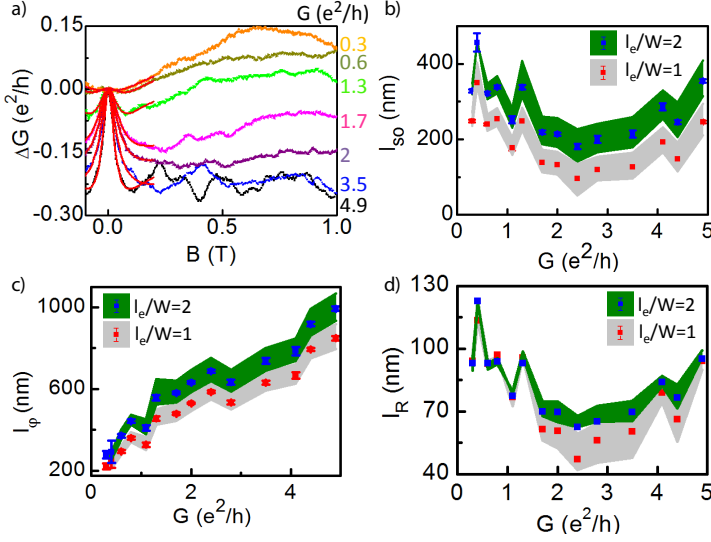
Figure 6.5: (a) Magnetoconductance (MC) obtained after averaging MC traces taken at the same G. For $G = 3.5, 1.3$ and $0.3 e^2/h$ the voltages at which these MC traces were taken are indicated in Fig. 6.4b. Averaged MC traces have been centered to $\Delta G = 0$ at $B = 0$ T. G ($B = 1$ T) is indicated on the right. Red curves are fits to the data assuming $\frac{l_e}{W} = 1$. (b) Spin relaxation length l_{so} obtained from the fits of panel (a) ($\frac{l_e}{W} = 1$, blue points) and obtained from fits with $\frac{l_e}{W} = 2$ (red points). Standard deviation of the fit outcomes is indicated. The distribution around the blue and red points (green and gray bands, respectively) is given by the spin-orbit lengths obtained from fits with an effective width 15 nm smaller (resulting in longer l_{so}) or larger (resulting in shorter l_{so}) than the expected wire width $W = 90$ nm. (c) Phase coherence length, l_φ and (d) spin precession length l_R as a function of device conductance. Figure formatting is as in panel (b).

At large G the magnetoconductance, measured with conductance controlled by the top gate at a temperature $T = 4.2$ K and with B perpendicular to the nanowire and substrate plane, shows an increase of conductance of ~ 0.2 to $\sim 0.3 e^2/h$ around $B = 0$ (Fig. 6.4e). $G(B)$ is, apart from reproducible conducantance fluctuations, flat at $B > 200$ mT, which is further evidence of specular boundary scattering.[26] On reducing conductance below $\sim 1.5 e^2/h$ WAL becomes less pronounced and a crossover to WL is seen.

Reproducible conductance fluctuations, most clearly seen at larger B (Fig. 6.4e), affect the WAL peak shape. To suppress these fluctuations several ($7 - 11$) MC traces are taken at the same device conductance (see Fig. 6.4b). After averaging these traces WAL remains while the

conductance fluctuations are greatly suppressed (Fig. 6.5a). Also here on reduction of conductance a crossover from WAL to WL is seen. Very similar results are obtained when averaging MC traces obtained as a function of top gate voltage with $V_{BG} = 0\,\mathrm{V}$. We expect that several (~ 10) subbands are occupied at device conductance $G \gtrsim 2\,e^2/h$ (see estimation in Sec. 6.4.4). Hence, our quasiclassical approach is valid and we fit the averaged MC traces to Eq. (6.1) with l_{so}, l_φ and the conductance at large magnetic field $\Delta G(B \to \infty)$ as fit parameters. l_{B} is extracted from Eq. (6.3). Wire diameter and mean free path are fixed in each fit, but we extract fit results for a wire diameter deviating from its expected value and for both $\frac{l_e}{W} = 1$ and $\frac{l_e}{W} = 2$. We find good agreement between data and fits (see Fig. 6.5a). While showing fit results covering the full range of G, we base our conclusions on results obtained in the quasiclassical transport regime $G \gtrsim 2e^2/h$.

On increasing conductance, the spin relaxation length first decreases to $l_{\mathrm{so}} \approx 100 - 200\,\mathrm{nm}$, then increases again to $l_{\mathrm{so}} \approx 200 - 400\,\mathrm{nm}$ when $G \geq 2.5e^2/h$ (Fig. 6.5b). The phase coherence length (Fig. 6.5c) shows a monotonous increase with device conductance. This increase can be explained by the density dependence of either the diffusion constant or the electron-electron interaction strength,[115] often reported as the dominant source of dephasing in nanowires.[86,114]

Spin relaxation[180] in our device can possibly occur via the Elliot-Yafet[55,182] or the D'yakonov-Perel' mechanism,[53] corresponding to spin randomization at or in between scattering events, respectively. The Elliot-Yafet contribution can be estimated as[39]

$$l_{\mathrm{so,EY}} = \sqrt{\frac{3}{8}\frac{E_G}{E_F}}\, l_e\, \frac{(E_G + \Delta_{\mathrm{SO}})(3E_G + 2\Delta_{\mathrm{SO}})}{\Delta_{\mathrm{SO}}(2E_G + \Delta_{\mathrm{SO}})} \geq 300 - 600\,\mathrm{nm}, \quad (6.15)$$

with band gap $E_G = 0.24\,\mathrm{eV}$, Fermi energy $E_F \leq 100\,\mathrm{meV}$, spin-orbit gap $\Delta_{\mathrm{SO}} = 0.8\,\mathrm{eV}$ and $\frac{l_e}{W} = 1 - 2$. For the D'yakonov-Perel' mechanism, we note that our nanowires have a zinc-blende crystal structure, grown in the [111] direction, where Dresselhaus SOI is absent for momentum along the nanowire.* We therefore expect that Rashba SOI is the dominant source of spin relaxation, in agreement with previous experiments.[129] As found in our theoretical analysis, it is then crucial to

---

*Furthermore, even for [100] nanowires Dresselhaus SOI is weak: In this case the maximum linear Dresselhaus SOI strength is γk_F^2 (with γ the cubic Dresselhaus SOI strength), yielding a spin-orbit length $l_{\mathrm{D}} = \hbar^2/m^*\gamma k_F^2$. With $\gamma = 437\,\mathrm{eV\,\mathring{A}}^3$[58] and $E_F \leq 100\,\mathrm{meV}$ we estimate $l_{\mathrm{D}} > 300\,\mathrm{nm}$.
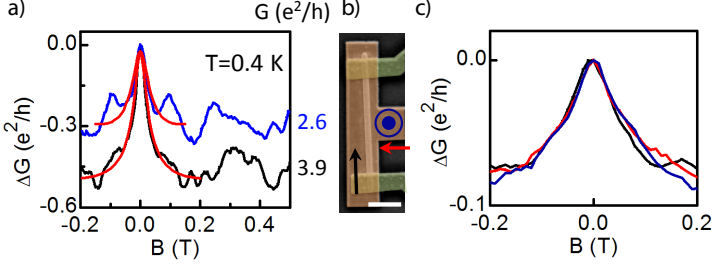
Figure 6.6: (a) Magnetoconductance (MC) at $T = 0.4$ K. Each MC trace is obtained after averaging 21 MC traces taken along the top-gate controlled pinch-off trace shown in Fig. 6.4c ($V_{BG} = 0$ V). Black (blue) trace is the average of traces taken between $V_{TG} = 0.34$ V and $V_{TG} = 0.14$ V ($V_{TG} = 0.12$ V and $V_{TG} = -0.08$ V) with steps of 20 mV. The voltage excitation V_{AC} was $10\,\mu V_{RMS}$. $G(B = 0.5$ T) is indicated on the right. Phase coherence and spin relaxation length obtained from fits (in red) to the traces is 1078 ± 32 (1174 ± 39) nm and of $95 \pm 18 (205 \pm 16)$ nm respectively for $\frac{l_e}{W} = 1$ (2). Values obtained at $G = 2.6 e^2/h$ are given below. (b) False color scanning electron microscope image of device II with different magnetic field orientations indicated by the arrows. Scale bar is $1\,\mu m$. (c) MC obtained with B parallel to the nanowire (in-plane angle w.r.t. nanowire $\theta \approx 5°$, black), B perpendicular to the nanowire in the plane of the substrate ($\theta \approx 95°$, red) and B perpendicular to the substrate plane (blue). $V_{TG} = 0.2$ V, $V_{BG} = 0$ V. Smaller ΔG compared to the preceding data is due to a larger contact resistance ($\sim 10 k\Omega$) of this device for which no correction was made.

capture confinement effects accurately. Our l_{so} correspond to $\frac{\tau_{so}}{\tau_e} = 2 - 15$ that are captured well by our simulations.[*]

Given that $W \approx l_R$, we extract the l_R corresponding to our $\frac{\tau_{so}}{\tau_e}$ directly from Fig. 6.2b. We extract spin precession lengths l_R of $50 - 100$ nm, shown in Fig. 6.5d, corresponding to $\alpha_R = 0.5 - 1.0$ eV Å. MC measurements on a second device show very similar l_R, see Fig. 6.15.

To confirm the interpretation of our MC measurements we extract MC at a lower temperature $T = 0.4$ K (Fig. 6.6a). We find larger WAL amplitudes of up to $\Delta G \sim 0.5 e^2/h$, while the width of the WAL peak remains approximately the same as at $T = 4.2$ K, corresponding to a longer l_φ at lower temperature, with approximately constant l_{so}. A longer l_φ is expected at lower temperature, as the rate of inelastic scattering, responsible for loss of phase coherence, is reduced in this regime.

Our theoretical analysis found similar dephasing times for magnetic fields perpendicular and parallel to the nanowire for our estimated

---

[*]Exceptions are the smallest values of l_{so} at $G = 2.4$ and $2.8 e^2/h$: When assuming a wire width larger than the expected value ($W = 105$ nm) we find $\frac{\tau_{so}}{\tau_e} \sim 1$. In this case the l_R corresponding to the lowest simulated value of $\frac{\tau_{so}}{\tau_e}$ have been chosen as a lower bound.

mean free paths, $l_e/W = 1 - 2$. Indeed, we observe virtually identical WAL for fields parallel and perpendicular to the nanowire in our second device (see Figs. 6.6b-c). WAL in the first device is also very similar for both field directions, see Fig. 6.13. This is in striking contrast to MC measurements in two-dimensional systems where only a perpendicular magnetic field gives strong dephasing due to orbital effects. It also provides strong support for the assumptions made in our theory, and emphasizes the importance of including the three-dimensional nature of nanowires to understand their MC properties. In contrast, WL is anisotropic, which we attribute to a different density distribution at low conductance compared to the high conductance at which WAL is seen.

Relevant to Majorana fermion experiments is the spin-orbit energy, $E_{SO} = \frac{m\alpha_R^2}{2\hbar^2}$, that is $0.25 - 1$ meV in our devices. These values compare favorably to InAs nanowires that yield $\alpha_R^{InAs} = 0.1 - 0.3$ eV Å [47,57,73,114,147] and corresponding $E_{SO}^{InAs} = 15 - 135 \,\mu$eV. E_{SO}^{InSb} is similar or slightly larger than reported spin-orbit energies in Ge/Si core-shell nanowires ($E_{SO}^{Ge/Si} = 90 - 600 \,\mu$eV [74,77]), while α_R^{InSb} is larger than $\alpha_R^{Ge/Si} = 0.07 - 0.18$ eV Å. Note that the device geometries and expressions for $\alpha_R(l_{so})$ used by different authors vary and that often only l_{so}, not l_R is evaluated. With our E_{SO} we then find, following the analysis of Ref. 154, a topological gap of $\sim 0.1 - 1$ K (details in Sec 6.4.5) even for our moderate mobilities of order 10000 cm^2/Vs. This gap largely exceeds the temperature and previous estimates. Hence, our findings underline the potential of InSb nanowires in the study of Majorana fermions.

6.4.1 Device fabrication

The nanowire is deposited onto a p^{++}-doped Si substrate covered by 285 nm SiO$_2$ (depicted in black in Fig. 6.4a). Contacts to the nanowire (green) are made by a lift-off process using electron beam lithography. Contact material is Ti/Au (25/125 nm). After passivation of the nanowire with a diluted ammoniumpolysulfur solution (concentration (NH$_4$)S$_X$:H$_2$O 1:200) the chip is covered with HfO$_2$ (30 nm), deposited by atomic layer deposition. The dielectric is removed at the bonding pads by the writing of an etch mask (PMMA) followed by an HF etch. A top gate (brown) is deposited using a lift-off process with electron beam lithography. Top gate is defined using Ti/Au (25/175 nm). Lastly, an additional layer of Ti/Pt (5/50 nm) is deposited on the bond pads to

reduce the chance of leakage to the global back gate. Devices were only imaged optically during device fabrication. SEM imaging was performed only after the measurements.

6.4.2 Estimation of mobility, mean free path and $\frac{l_e}{W}$

Nanowire mobility, μ, is obtained from pinch-off traces using the method described in section 3 of the Supplementary Material of Ref. 140. In short, mobility is obtained from the change of current, or conductance, with gate voltage. We thus extract field-effect mobility, whereby we rely on a fit of the gate trace to an expression for gate-induced transport. This expression includes a fixed resistance in series with the gated nanowire. To extract mobility and series resistances from device I (data shown in Fig. 6.4–6.6a as well as Fig. 6.7, Fig. 6.11, Fig. 6.12, Fig. 6.13, Fig. 6.14) in this way, a gate trace from pinch-off to saturation is needed. However, $I(V_{BG}, V_{TG} = 0\,\text{V})$ obtained from Fig. 6.7a covers only an intermediate range (see 6.7b). Therefore traces at $I(V_{BG}, V_{TG} = -0.15,\text{V})$ and $I(V_{BG}, V_{TG} = 0.15\,\text{V})$, shown in Fig. 6.7b are also used. The three traces then together form a full pinch-off trace (see Fig. 6.7c) that is well approximated by Eq. (11) in Ref. 140, for which here an equivalent expression for current I instead of conductance G was used. Here the capacitance between back gate and nanowire $C_{BG} = 22\,\text{aF}$, the series resistance $R_S = 10\,\text{k}\Omega$, the mobility $\mu = 12,500\,\text{cm}^2/\text{Vs}$ and the threshold voltage $V_{TG} = -16.5\,\text{V}$ (see Fig. 6.7c). Other inputs are source-drain bias $V_{SD} = 10\,\text{mV}$ and contact spacing $L = 2\,\mu\text{m}$. The capacitance has been obtained from electrostatic simulations in which the hexagonal shape of the nanowire has been taken into account. The series resistance R_S consists of instrumental resistances (RC-filters and ammeter impedance, together $8\,\text{k}\Omega$) and a contact resistance R_C. The experimental pinch-off traces are best approximated by $R_C = 2\,\text{k}\Omega$. Expressions for $I(V_{BG})$ with $R_C = 1\,\text{k}\Omega$ and $R_C = 3\,\text{k}\Omega$, also shown in Fig. 6.7c, deviate from the measured pinch-off traces. Mobility is also estimated from a linear fit to the top gate pinch-off trace shown in Fig. 6.7d. Prior to this fit instrumental and series resistances have been subtracted. From the fit $\mu \sim 9,000\,\text{cm}^2/\text{Vs}$ is obtained, using $C_{TG} = 1440\,\text{aF}$, obtained from electrostatic simulations, and $L = 2\,\mu\text{m}$. Similarly, mobility in device III (see Fig. 6.7e, magnetoconductance data shown in Fig. 6.15 is extracted from a fit to the top gate pinch-off trace, giving $\mu \sim 10000\,\text{cm}^2/\text{Vs}$ using $C_{TG} = 1660\,\text{aF}$ and $L = 2.3\,\mu\text{m}$. These mobilities are similar to those
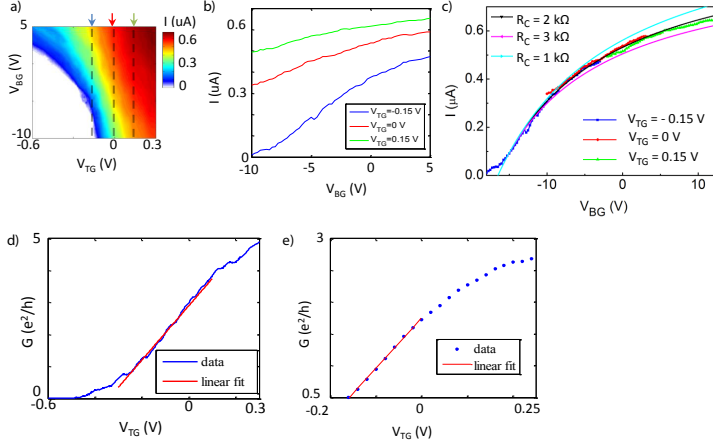
Figure 6.7: (a) Current, I, in device I as a function of top gate voltage, V_{TG}, and back gate voltage, V_{BG}. Cross sections corresponding to the $I(V_{BG})$ traces in panel b are indicated with arrows. Data taken with source-drain voltage $V_{SD} = 10\,\text{mV}$. (b) $I(V_{BG})$ at $V_{TG} = 0.15\,\text{V}$, $V_{TG} = 0\,\text{V}$ and $V_{TG} = -0.15\,\text{V}$. (c) Traces at $I(V_{BG}, V_{TG} = -0.15\,\text{V})$ (blue) and $I(V_{BG}, V_{TG} = 0.15\,\text{V})$ (green) are displaced by $\Delta V_{BG} = -8\,\text{V}$ and $\Delta V_{BG} = 8\,\text{V}$, respectively, chosen such that their current is similar to that of the $I(V_{BG}, V_{TG} = 0\,\text{V})$ trace (red). Data is well approximated by $I(V_{BG})$ (see text) with mobility $\mu \sim 12,500\,\text{cm}^2/\text{Vs}$ and contact resistance $R_C = 2\,\text{k}\Omega$ (black). Traces with larger ($3\,\text{k}\Omega$, pink) or smaller ($1\,\text{k}\Omega$, cyan) contact resistance are also shown. (d) $G(V_{TG})$ in device I with $V_{BG} = 0\,\text{V}$ (blue). A linear fit of the pinch-off traces (red) gives a slope $\frac{dG}{dV_{TG}} = 8.5(e^2/h)/\text{V}$. (e) $G(V_{TG})$ in device III with $V_{BG} = 0\,\text{V}$. A linear fit of the pinch-off traces (red) gives a slope $\frac{dG}{dV_{TG}} = 7.9(e^2/h)/\text{V}$.

obtained in InSb nanowires that are gated using only a global back gate.[140] Mean free path, l_e, is estimated as $l_e = v_F \tau_e$, with v_F the Fermi velocity and τ_e the scattering time. $\tau_e = \frac{\mu m^*}{e}$, with e electron charge and m^* the effective electron mass in InSb. Assuming a 3D density of states $v_F = \frac{\hbar}{m^*}(3\pi^2 n)^{\frac{1}{3}}$ with $\hbar$ the reduced Planck constant and n electron density, n is estimated from pinch off traces using $n = \frac{C(V_G - V_{TH})}{eAL}$ with A the nanowire cross section, V_G top or back gate voltage and V_{TH} the threshold (pinch-off) voltage. In this way in device I n up to $\sim 4 \cdot 10^{17}\,\text{cm}^{-3}$ are obtained, giving l_e up to $\sim 160\,\text{nm}$. This estimate of n agrees reasonably with densities obtained from a Schrödinger-Poisson solver (see Subsec. 6.4.4). In device III n up to $\sim 4 \cdot 10^{17}\,\text{cm}^{-3}$ gives $l_e \sim 150\,\text{nm}$. Together with the facet-to-facet width W (described in Fig. 6.8) these mean free paths yield a ratio $\frac{l_e}{W} = 1 - 2$.

6.4.3 Nanowire width

Nanowires were not imaged with scanning electron microscope prior to device fabrication to avoid damage due to electron irradiation. The wire diameter is estimated from a comparison of the nanowire width after fabrication to the nanowire diameter obtained from a number of wires from the same growth batch deposited on a substrate as described in Fig. 6.8.

6.4.4 Estimation of the number of occupied subbands

An estimate of the number of occupied subbands is calculated in two ways:

1. A self-consistent Schrodinger-Poisson calculation yields that 17 subbands contribute to transport at higher device conductance (density profile shown in the inset of Fig. 6.9). As contact screening has been neglected in these two-dimensional calculations the actual number of subbands may be slightly lower, but likely several (~ 10) modes contribute at high device conductance.

2. The conductance, G, of a disordered quantum wire relates to the number of subbands, N, as[20]

$$G = \frac{N G_0}{1 + \frac{L}{l_e}},\qquad(6.16)$$

   which, using $\frac{L}{l_e} \approx 10 - 20$ (obtained from the estimate of l_e above) yields $N \geq 25$.

6.4.5 Topological gap as a function of mobility and spin-orbit strength

We follow the theoretical analysis of Ref. 154 to compute the maximum topological gap that can be achieved at a given mobility μ and spin-orbit strength α_R. One should only be careful to note that the definition of E_{SO} in Ref. 154 differs by a factor of 4 from ours. Whenever we refer to E_{SO} here, we use our definition given in Sec. 6.4.
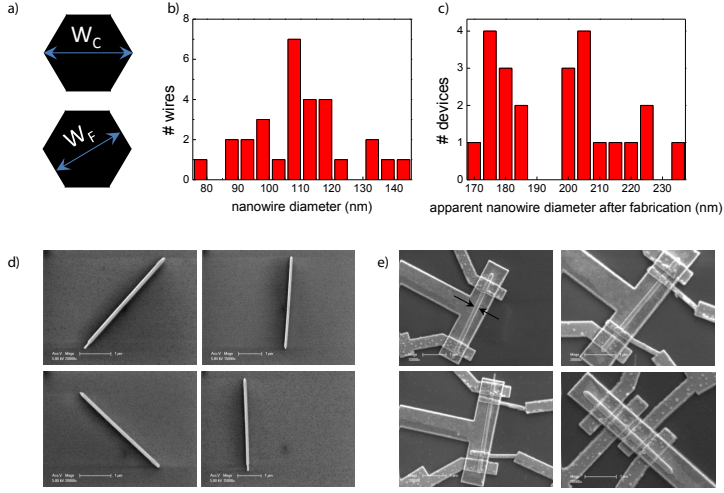
Figure 6.8: (a) Cross-sectional view of hexagonal nanowires with indicated widths W_C and W_F. A top view of these nanowires (such as a scanning electron microscope image) shows the width from corner to corner, W_C. In our simulations of electron interference in hexagonal nanowires the facet-to-facet width, W_F, is used. The two widths are related by $W_F = \cos(\frac{\pi}{6})W_C$. (b) Distribution of nanowire diameters obtained from scanning electron microscope images of nanowires lying on a substrate. The imaged nanowires are from the same growth batch as the ones used in the experiment. The nanowire diameter is the width of the nanowire when lying on a substrate and thus corresponds to W_C in panel a plus twice the native oxide thickness. Four imaged wires are shown in panel d. Average diameter is 110 nm, standard deviation is 15 nm. (c) Distribution of the apparent nanowire diameter after device fabrication. The distribution has been obtained from scanning electron microscope images of devices made in the same fabrication run (and thus with the same fabrication recipe) as the ones measured. The apparent diameter increases due to HfO_2 and top gate metal deposition. Average apparent diameter is 197 nm. Device I had an apparent diameter after fabrication of 200 nm, close to the average apparent nanowire device diameter, and therefore its wire diameter is estimated as 110 nm, the average the distribution of wire diameters in panel c. Device III has a diameter after fabrication of 180 nm, which is 17 nm below average. Wire diameter is therefore estimated as $110 - 17 = 93$ nm. Wires are covered by a native oxide of ~ 2.5 nm, giving an InSb diameter $W_C \approx 105$ nm and $W_C \approx 88$ nm for device I and device III respectively. Facet-to-facet diameter W_F, simply denoted by W in the previous sections, is therefore $W \approx 90$ nm (device I) and $W_F = W \approx 75$ nm (device III). The standard deviation of wire diameter of 15 nm in panel b is used to define a range of wire diameters, $W \pm 15$ nm, for which spin relaxation length, spin precession length and phase coherence length are obtained in Fig. 6.5. (d) Scanning electron microscope image of four of the nanowires used to obtain the histogram of nanowire diameters of panel b. (e)Scanning electron microscope image of four of the devices imaged to obtain the apparent nanowire diameter after fabrication of panel c. The arrows in the upper left image indicate the apparent nanowire diameter.

In Fig. 6.10a we show the topological gap as a function of mobility for the spin-orbit energies estimated in the main text, with parameters suitable for the Majorana experiments in Ref. 128 We observe a nearly linear dependence of the topological gap on mobility for these parameters.
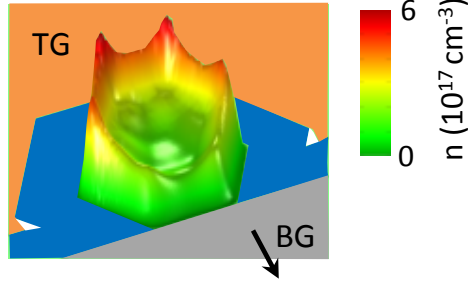
Figure 6.9: Electron density as a function of the nanowire cross section. Density is obtained from self-consistent Schrodinger-Poisson calculations with $V_{TG} = 0.5$ V and $V_{BG} = 0$ V. TG (BG) denotes top (back) gate.
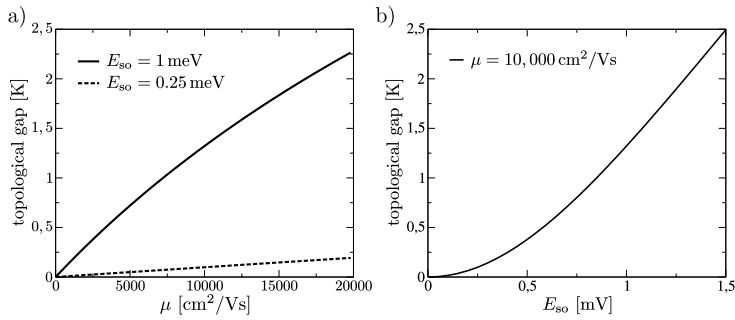

Figure 6.10: (a) Topological gap as a function of mobility for different values of E_{so}. (b) Topological gap as a function of E_{so} for a fixed mobility of 10000 cm^2/Vs. The remaining parameters were chosen to be suitable for InSb nanowires in proximity to NbTiN: effective mass $m^* = 0.014\,m_e$ and superconducting gap $\Delta = 30$ K.

The topological gap can be rather sizable, and we find gaps of order $1\,\mathrm{K}$ for a moderate mobility of $\mu = 10{,}000\,\mathrm{cm}^2/\mathrm{Vs}$ for $E_{\mathrm{so}} = 1\,\mathrm{meV}$. From the figure it is also apparent that the topological gap depends rather strongly on E_{so}.

We investigate the E_{so}-dependence of the topological gap in Fig. 6.10b. At a mobility of $10{,}000\,\mathrm{cm}^2/\mathrm{Vs}$ the topological gap depends roughly quadratically on E_{so} up to $E_{\mathrm{so}} \sim 1\,\mathrm{meV}$, i.e. the topological gap increases as α_R^4. This is in stark contrast to the clean case where the topological gap depends linearly on α_R.

The different dependences of the topological gap on mobility (linear) and spin-orbit strength (to the fourth power) indicates that for current devices it may be more efficient to attempt to improve spin-orbit strength rather than mobility.
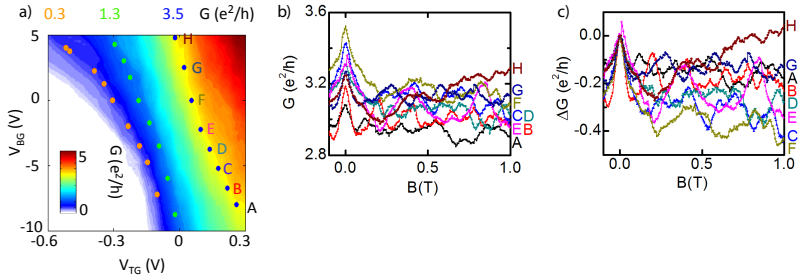
6.5 Supplementary experimental data

Figure 6.11: Magnetoconductance traces at constant conductance. (a) Conductance G, as a function of top gate voltage, V_{TG}, and back gate voltage, V_{BG} as shown in Fig. 6.4b. Dots indicate voltages (V_{BG},V_{TG}) at which traces in Fig. 6.5a were taken (same dot color corresponds to same G). The letters at the dots at $G = 3.5e^2/h$ refer to the magnetoconductance traces shown in panels b and c. Data obtained with 10 mV voltage bias at a temperature of 4.2 K. (b) Magnetoconductance traces taken at the points at $G = 3.5e^2/h$ shown in panel b. Data taken with AC excitation $V_{AC} = 100\,\mu\mathrm{V}_{RMS}$. The difference between the conductance of the dots in panel a and the conductance of the corresponding magnetoconductance traces in panel b is likely due to the difference in source-drain bias between both measurements. Also at other conductances (for instance at the green and orange dots in panel a) magnetoconductance traces generally show a conductance lower than those obtained in the gate-gate plot of panel a by a similar amount. For each of these traces the conductance denoted on the vertical axis of Fig. 4a and that on the horizontal axis of Fig. 4b-d is the conductance of the equiconductance points of Fig. 6.4b. (c) Magnetoconductance traces of panel b normalized to $\Delta G(B = 0) = 0$. By averaging over these traces the blue trace of Fig. 6.5a ($G = 3.5e^2/h$) is obtained.
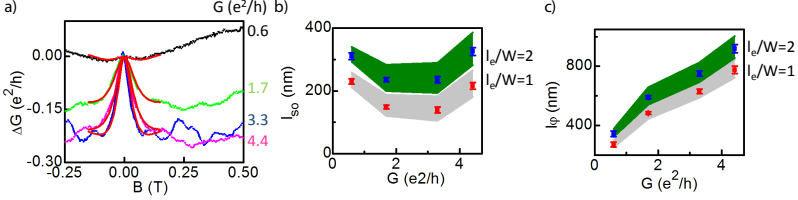
Figure 6.12: Spin relaxation and phase coherence length obtained from top gate averaging in device I (a) Magnetoconductance traces obtained after taking MC traces with top gate voltage spacing $\Delta V_{TG} = 20\,\text{mV}$ between $V_{TG} = 0.34\,\text{V}$ and $V_{TG} = -0.42\,\text{V}$ and averaging 9 subsequent traces. $V_{BG} = 0\,\text{V}$. Averaged MC traces have been centered to $\Delta G = 0$ at $B = 0\,\text{T}$. $G(B = 0.5\,\text{T})$ is indicated on the right. Red curves are fits to Eq. (6.1), wherein Eqs. (6.2) and (6.3) have been used to obtain l_B, using $l_e/W = 2$ and $W = 90\,\text{nm}$. (b) Spin relaxation length, l_{so}, obtained from the fits of panel a ($\frac{l_e}{W} = 2$, red points) and obtained from fits with $\frac{l_e}{W} = 1$ (blue points). Standard deviation of the fit outcomes are indicated. The distribution around the blue and red points (in green and gray, respectively) is given by the spin-orbit lengths obtained from fits with an effective width 15 nm smaller or larger than the expected wire width $W = 90\,\text{nm}$. (c) Phase coherence length, l_φ, obtained from fits of panel a. Figure formatting (colors, standard deviation and wire diameter dependence) is the same as in panel b.

(e^2/h)	$\frac{l_e}{W}$	l_{so} (nm)	l_φ (nm)
3.9	1	95 ± 18	1078 ± 32
	2	205 ± 16	1174 ± 39
2.6	1	171 ± 26	805 ± 52
	2	380 ± 29	937 ± 60

Table 6.1: Phase coherence and spin relaxation length at $T = 0.4K$**.** Spin relaxation length, l_{so}, and phase coherence length, l_φ, obtained from fits to the traces in Fig. 6.5a. $\frac{l_e}{W}$ denotes the ratio of mean free path, l_e, to wire width, W.
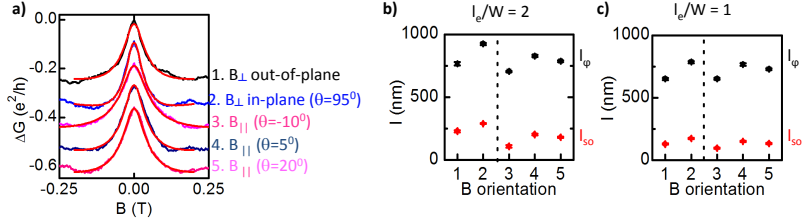
Figure 6.13: Magnetoconductance in parallel and perpendicular field in device I. (a) MC with parallel and perpendicular magnetic field orientation. Out-of-plane, $\perp$, (in-plane, $\parallel$,) denotes an orientation of the magnetic field (parallel) perpendicular to the substrate plane. θ denotes the in-plane angle of the magnetic field w.r.t. the nanowire. As the uncertainty in orientation of the in-plane magnetic field is 20° three parallel magnetoconductance traces with $|\theta| \leq 20°$ are shown. Each MC trace is an average of 7 traces taken at the same conductance $G = 3.5\,e^2/h$ by varying top and back gate voltage similar to the MC data of Fig. 6.2. No systematic change of MC along these equiconductance points was observed. As in device II (Fig. 6.6c) also here WAL in parallel and perpendicular magnetic field are very similar. Red curves are fits to Eq. (6.1) (in which Eqs. (6.2) and (6.3) have been used for l_B, with values of C corresponding to parallel or perpendicular magnetic field orientation), using $\frac{l_e}{W} = 1$ and $W = 90\,\text{nm}$. (b) Spin relaxation length (red) and phase coherence length (black) obtained from fits of the MC traces in panel a using $\frac{l_e}{W} = 2$. B orientation numbers correspond to the traces numbered 1 to 5 in panel a. (c) Spin-orbit length (red) and phase coherence length (black) obtained from fits of the MC traces in a using $\frac{l_e}{W} = 1$. The slightly wider WAL peak in parallel magnetic field yields better agreement with $\frac{l_e}{W} = 1$ as spin-orbit lengths and phase coherence lengths obtained in parallel and perpendicular field with $\frac{l_e}{W} = 1$ are more similar than when assuming $\frac{l_e}{W} = 2$.
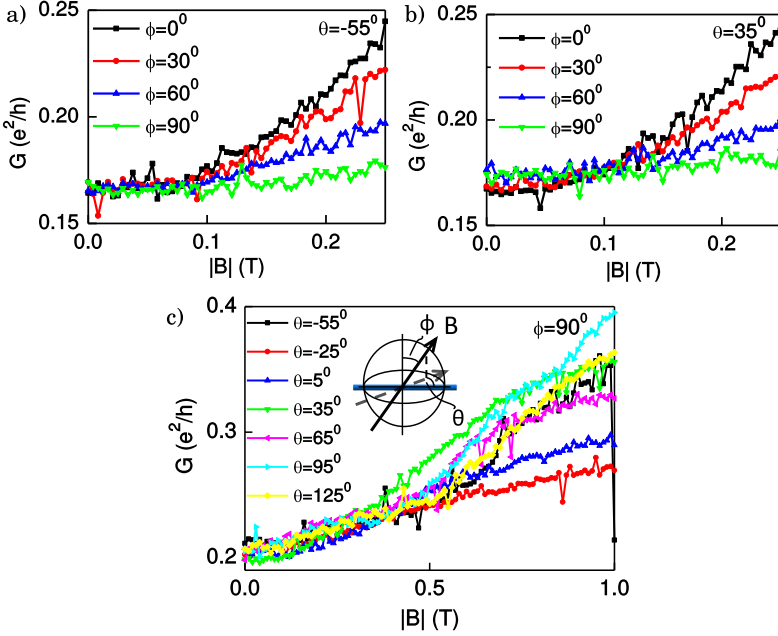
Figure 6.14: Magnetoconductance for other angles of magnetic field in device I. (a) MC as a function of out-of-plane angle, ϕ, with in-plane angle w.r.t. the nanowire $\theta = -55 \pm 20°$. Angles θ and ϕ are shown in the schematic drawing in the inset of panel c. Out-of-plane (in-plane) denotes an orientation of the magnetic field (parallel) perpendicular to the substrate plane. $\phi = 0°$ (90°) is magnetic field perpendicular to (parallel to) the substrate plane. (b) MC as a function of out-of-plane angle ϕ with in-plane angle w.r.t. nanowire $\theta = 35 \pm 20°$. While weak anti-localization is (nearly) independent of magnetic field orientation, here we find that the suppression of weak localization by the magnetic field becomes less effective when rotating the field from perpendicular to parallel to the substrate plane. (c) MC as a function of in-plane angle θ. Although the suppression of weak localization by magnetic field is much less effective for all magnetic fields oriented parallel to the substrate plane, a closer inspection shows that the magnetic field dependence is weakest when the magnetic field is approximately aligned with the nanowire. We suggest that the difference in dependence on magnetic field orientation between WAL and WL is due to a difference in charge distribution: while at the larger device conductance at which weak anti-localization is observed many subbands all across the nanowire cross section contribute to transport (see the inset of Fig. 6.2d), at low conductance, when weak localization is seen, transport takes place only a few modes, confined to a small region of the nanowire cross section. The low conductance situation may resemble a two-dimensional system, in which only the magnetic field component perpendicular to the substrate leads to a suppression of WL. This would lead to the reduction of positive MC when rotating the magnetic field from out-of-plane to in-plane. In all panels $V_{TG} = -0.36$ V, $V_{BG} = 0$ V. The difference in $G(B = 0$ T) between panels a-b and c is due to a slight device instability at low conductance or due to hysteresis when sweeping V_{TG}.
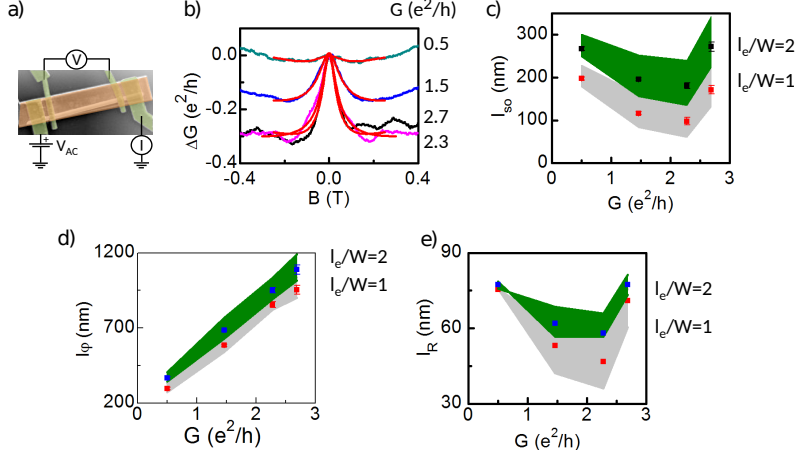
Figure 6.15: Device III: Reproducibility of extracted spin relaxation and phase coherence length. (a) False color scanning electron microscope image of device III. A voltage bias, V_{AC}, is applied across the outer contacts, after which simultaneously the current, I, through the device and the voltage across the inner contacts, V, is measured. Subsequently conductance $G = \frac{I}{V}$ is determined. (b) Averaged MC traces obtained after taking MC traces with top gate voltage spacing $\Delta V_{TG} = 20\,\text{mV}$ between $V_{TG} = 0.3\,\text{V}$ and $V_{TG} = -0.22\,\text{V}$ and averaging 7 subsequent traces. $V_{BG} = 0\,\text{V}$. $G(|B| = 0.5\,\text{T})$ is indicated. Red curves are fits to Eq. (6.1), wherein Eqs. (6.2) and (6.3) have been used to obtain l_B, using $l_e/W = 1$ and $W = 75\,\text{nm}$. (c) Spin relaxation length, l_{so}, obtained from the fits of panel b ($\frac{l_e}{W} = 1$, blue points) and obtained from fits with $\frac{l_e}{W} = 2$ (red points). Standard deviation of the fit outcomes is indicated. The distribution around the blue and red points (in green and gray, respectively) is given by the spin-orbit lengths obtained from fits with an effective width 15 nm smaller or larger than the expected wire width $W = 75\,\text{nm}$. (d) Phase coherence length, l_φ, obtained from the fits of panel b ($\frac{l_e}{W} = 1$, blue points) and obtained from fits with $\frac{l_e}{W} = 2$ (red points). Figure formatting is the same as in panel c. (e) Spin precession length, l_R, as a function of device conductance, G, extracted from the spin relaxation lengths of panel c. Figure formatting is the same as in panel c. When assuming $W = 90\,\text{nm}$ the $\frac{\tau_{so}}{\tau_e}$ corresponding to the l_{so} at $G = 2.3e^2/h$ are below the simulation range. In this case the l_R corresponding to the lowest simulated value of $\frac{\tau_{so}}{\tau_e}$ has been chosen.